Journal of Alloys and Compounds 976 (2024) 173051

Contents lists available at ScienceDirect

Journal of Alloys and Compounds

journal homepage: www.elsevier.com/locate/jalcom

Improvement of the rate capability of the $Li_4Ti_5O_{12}$ anode material by modification of the surface composition with lithium polysulfide

Julián Cáceres-Murillo [a], Pilar Díaz-Carrasco [a], Alois Kuhn [a], Enrique Rodríguez-Castellón [b], Flaviano García-Alvarado [a,*]

[a] Departamento de Química y Bioquímica, Facultad de Farmacia, Universidad San Pablo-CEU, CEU Universities, Urbanización Montepríncipe, 28668 Boadilla del Monte, Madrid, Spain

[b] Departamento de Química Inorgánica, Cristalografía y Mineralogía (Unidad Asociada al ICP-CSIC), Facultad de Ciencias, Universidad de Málaga, Campus de Teatinos, 29071 Málaga, Spain

ARTICLE INFO

Keywords:
Lithium-ion anode
LTO
Spinel
Lithium titanate
XPS

ABSTRACT

Partial substitution of oxygen by sulfur was attempted using a Li/Ti rich conditions for the nominal compositions $Li_4Ti_5O_{12-x}S_x$ x = 0.125–0.375. However, a much lower sulfur substitution, i.e. at dopant level, was achieved as deduced from an almost negligible increase in unit cell size observed from X-ray powder diffraction. The sulfur in the samples is mainly deposited on the surface as sulfate and Li_2S_2 as deduced from XPS. However, most of the nominal sulfur is lost. Interestingly, for nominal x = 0.125 a considerable improvement in performance is achieved compared to undoped LTO. The sample with x = 0.125 not only shows ~9% higher capacity at slow cycling at C/20, but also has a remarkably better power rate behavior, with a capacity of 125 mAh g^{-1} at higher 2 C, compared to 79 mAh g^{-1} for LTO at the same rate. The significant improvement is explained by the formation of lithium polysulfide in the high-temperature reaction and the concomitant Li^+ deficiency to form the spinel, causing the reduction of Ti^{4+} to Ti^{3+} and the creation of oxygen vacancies with the formation of an oxygen and lithium deficient spinel $Li_{4-y}(Ti^{4+})_{5-y}(Ti^{3+})_y O_{12-y}$. Li_2S_2, detected in the sample with nominal x = 0.125 by XPS and at higher nominal sulfur contents by CV, may prevent carbonation of the spinel surface while providing ionic conductivity upon reduction to Li_2S, justifying its better performance. On the other hand, the contribution to capacity from both mass diffusion and the capacitive charge storage mechanism is unaffected, and therefore LTO and surface-modified LTO-S-0.125 are regarded as typical battery materials.

1. Introduction

Several properties make $Li_4Ti_5O_{12}$ (LTO) one of the most promising materials for use as an anode in lithium electrochemical energy storage: zero-strain behavior with negligible volume change during lithium insertion/extraction for long cycle life; safe material due to its relatively high intercalation potential compared to graphite and its high thermal stability; a cheap material that is easy to prepare from earth-abundant transition metal sources [1–3]. Although its low electronic conductivity ($\sim 10^{-8}$ -10^{-13} S cm^{-1}) [4–7] is a disadvantage, a high diffusion coefficient for Li^+ ions has been reported. Zaghib *et al.* estimated a value of $2 \bullet 10^{-8}$ cm^2 s^{-1} from CV data [8], while Yan *et al.* found that at 1.6 V, this is in the single-phase $Li_{4+x}Ti_5O_{12}$ domain, D_{Li} is $2.94 \bullet 10^{-9}$ cm^2 s^{-1} [6]. However, Yuan *et al.* reported a much lower value of $2.8 \bullet 10^{-13}$ cm^2 s^{-1}, also at 1.6 V [4]. Various strategies have been pursued to further improve the performance, mainly by increasing the electrical conductivity or diffusivity, such as particle size reduction [9], [10], doping [11], [12], composite formulation [13], [14] and carbon coating [15].

Most of the studies on doping LTO have focused on the substitution of structural Li, Ti or both sites by other metals; $Li_{4-x}Na_xTi_5O_{12}$ [16], $Li_{4-x}Mg_xTi_5O_{12}$ [5], $La_{0.06}Li_{3.94}Ti_5O_{12}$ [17], $Li_4Ti_{5-x}Al_xO_{12}$ [18], $Li_4Ti_{5-x}P_xO_{12}$ [19], $Li_4Ti_{4.95}V_{0.05}O_{12}$ [20] or $Li_{4-x}Mg_xTi_{5-y}Zr_yO_{12}$ [21] among others. However, there are only a few reports on anion doping to obtain a mixed anion compound $Li_4Ti_5O_{12-y}X_y$; $Li_4Ti_5Br_xO_{12-x}$ [22], $Li_4Ti_5O_{12-x}F_x$ [23], $Li_4Ti_5O_{12-x}Cl_x$ [24], $Li_4Ti_5O_{12-x}(PO_4)_x$ [25] or $Li_4Ti_5O_{12-x}F_x$/C [26]. For example, Bai *et al.*[23] reported that fluoride can replace oxide ions in the LTO structure according to the compositions $Li_4Ti_5O_{12-x}F_x$ with x = 0.1, 0.2 and 0.3. $Li_4Ti_5O_{11.9}F_{0.1}$ showed the best cyclability, the highest specific capacity (165 mAh g^{-1} at 0.2 C)

* Corresponding author.
E-mail address: flaga@ceu.es (F. García-Alvarado).

https://doi.org/10.1016/j.jallcom.2023.173051
Received 21 August 2023; Received in revised form 5 November 2023; Accepted 2 December 2023
Available online 5 December 2023

Table 1
Specific capacity of selected LTO samples with partial substitution of the oxide ions.

Samples	Nominal x	Specific capacity/ mAh g^{-1}	Specific capacity of reference LTO / mAh g^{-1}	Ref.
$Li_4Ti_5Br_xO_{12-x}$	0.5	143 at 1 C	~131 at 1 C	[22]
$Li_4Ti_5O_{12-x}F_x$	0.1,	165 at 0.2 C	~150 at 0.2 C	[23]
$Li_4Ti_5O_{12-x}Cl_x$	0.2	133 at 1 C	110.9 at 1 C	[24]
$Li_4Ti_5O_{12-x}(PO_4)_x$	0.02	171 at 0.1 C	153.4 at 0.1 C	[25]
$Li_4Ti_5O_{12-x}F_x$/C	0.3	325.6 at 170 mA g^{-1}	205.5 at 170 mA g^{-1}	[26]
$Li_4(Ti_{5-x}S_x)_5O_{12}$	-	175 at 1.0 C	136.6 at 1 C	[27]

compared to LTO (150 mAh g^{-1}), the lowest charge transfer resistance (56.4 Ω for $Li_4Ti_5O_{11.9}F_{0.1}$ and 80.6 Ω for LTO), and a similar diffusion coefficient (2.505 • 10^{-10} cm^2 s^{-1} and 1.694 • 10^{-10} cm^2 s^{-1}, respectively). Jun *et al.* [22] reported the partial substitution of oxide by bromide, according to the nominal composition $Li_4Ti_5O_{12-x}Br_x$ (x = 0.1, 0.3, 0.5 and 0.7). Interestingly, the mostly surface bromine resulted in improved electrical conductivity. Samples with lower nominal bromine (x = 0.1, 0.3 and 0.5) showed slightly better specific capacities (138mAh g^{-1}, 140 mAh g^{-1} and 143 mAh g^{-1}, respectively) than the reference LTO sample (~131 mAh g^{-1}) at 1 C. Table 1 gives a brief summary of the best specific capacities reported in the cases described here and some others found in the literature on oxide ion substitution.

Sulfur doping, on the other hand, has not been studied so extensively. In fact, there are only a few reports [27–29] and some found no evidence of O/S substitution. Shen *et al.* [27] found a significant improvement in performance after treating a 1:1 w/w mixture of LTO and thiourea under an argon atmosphere at 500 ºC. Preferred doping sites were investigated by DFT calculations, concluding that sulfur doping at the 16*d* Ti site is more favorable (lower defect formation energy) due to the oxygen-rich (titanium-poor) conditions provided by thiourea. Experimental results confirmed the substitution at the 16*d* Ti position and the improvement in specific capacity (see Table 1) with respect to their reference LTO sample. Furthermore, rate and cycling performance (126.4 mAh g^{-1} after 1000 cycles at 20 C) were also benefited by the substitution. The S doping level was reported to be 1.4 at% on the surface as determined by XPS. Despite an apparently low doping level, the authors claimed that the improvement in capacity could be due to a decrease in band gap, an increase in lattice spacing and an increase in both Ti^{3+} and oxygen vacancies. Interestingly, DFT calculations suggested that substitution at the 32*e* O site would instead be favored under Li/Ti rich conditions. Both possibilities are supported by the reports on S-substitution in [30–33].

In this work, the partial substitution of oxygen by less electronegative sulfur was attempted to increase the covalency of the M-ligand bond and thus, decrease the lithium intercalation potential. Based on the predictions of Shen *et al.* [27], Li/Ti rich conditions were used in the synthesis procedure. XRD and microanalysis of the ceramic samples indicate that O/S anion substitution occurs at much lower extent than nominal, only at the dopant level, while XPS confirms the presence of lithium polysulfide on the surface, which has a strong influence on the performances, particularly on the rate capability of the obtained spinel.

2. Material and methods

Samples of nominal composition $Li_4Ti_5O_{12-x}S_x$ (x = 0, 0.125, 0.250 and 0.375) were targeted by the ceramic method. Stoichiometric quantities of the following reagents were used: Li_2CO_3 (Aldrich, 99.8%), TiO_2 (anatase, Aldrich, 99.8%) and TiS_2 (Aldrich, 99.9%), the latter being used as the sulfur source. Li_2CO_3 and anatase TiO_2 were first mixed and ground and decarbonated at 730ºC for 10 h. For $Li_4Ti_5O_{12}$ the mixture was heated at 900ºC. For $Li_4Ti_5O_{12-x}S_x$ (x = 0.125, 0.250 and 0.375) the required amount of TiS_2 was then added to create a Li/Ti-rich condition, and the mixture was ground and pelletized. The pellets were placed in a quartz tube sealed under vacuum and heated at 900ºC for 7 h. The samples are designated as LTO-S-x, where x is the nominal sulfur content.

Structural characterization was performed by powder X-ray diffraction (PXRD) using a Bruker D8 high-resolution diffractometer equipped with a LynxEye solid-state fast detector, with monochromatic CuKα1 (λ = 1.5406 Å) radiation. Diffraction patterns were recorded in the range 2θ = 10–80º and analyzed by Rietveld refinement using the FullProf program [34]. The morphology of the samples was studied by scanning electron microscopy, using a Thermo Fisher Scientific Prisma E microscope, while the sulfur content was determined by using energy dispersive X-ray spectroscopy (X-EDS). X-ray photoelectron spectroscopy (XPS) studies were performed on a Physical Electronics PHI VersaProbe II spectrometer using monochromatic Al-Kα radiation (49.1 W, 15 kV and 1486.6 eV) to analyse the core-level signals of the elements of interest with a hemispherical multi-channel analyzer. The sample spectra were recorded with a constant pass energy value of 29.35 eV, using circular analysis area of 100 μm diameter. The resulting X-ray photoelectron spectra were analyzed using PHI SmartSoft software and processed using the MultiPak 9.5 package. The binding energy values were referenced to adventitious carbon C 1 *s* signal (284.8 eV). Shirley type background and Gauss-Lorentz curves were used to determine the binding energies.

Samples were analyzed using the Spectrum Two Perkin Elmer Fourier Transform (FTIR) Spectrometer equipped with an Attenuated Total Reflectance (ATR) internal reflection system in the 4000–500 cm^{-1} wave number range. The resolution of the spectra was 4 cm^{-1}, and the data were collected in the transmittance mode.

For electrochemical studies working electrodes were prepared with LTO-S-x as the active material. Slurries containing the active materials, polyvinylidene fluoride (PVDF) and SuperC65 carbon in a 8:1:1 wt ratio, respectively, were tape cast onto a copper foil. Electrodes with a diameter of 12 mm were punched and dried at 60 °C. Lithium metal was used as both the reference and counter electrode and a glass fibre disk (Whatman type D) as a separator. The electrolyte was 1 M $LiPF_6$ in EC/DMC in a volume ratio of 1:1 (Solvionic). The electrochemical properties of the LTO-S-x samples were evaluated in CR2032 coin cells assembled in an Ar-filled glove box (O_2 and H_2O < 0.1 ppm). The cells were run using a VMP3 multi-channel system (BioLogic). Cyclability was investigated by successive galvanostatic discharge/charge cycles at C/20 and C/5 rates, which are the currents required to insert a lithium ion in 20 h and 5 h, respectively. The response of the electrode at higher current rates was investigated by recording the discharge capacity developed over 5 cycles at different current rates ranging from C/20–2 C. Potentiostatic Electrochemical Impedance Spectroscopy (PEIS) was used to assess the variation in charge transfer (CT) and cathode electrolyte interphase (CEI) resistances and the Warburg coefficient at different potentials. Impedance measurements of working electrode were carried out in three-electrode cells in the range of 1 MHz to 1 mHz, using lithium metal as both the reference and counter electrode and tape cast slurries of LTO or LTO-S-x samples as the working electrode. Each cell was left to equilibrate at 25º for 2 h. Impedance measurements with an AC voltage of 10 mV were made before discharging. Cells were then discharged to different voltages by applying a constant current equivalent to C/20 rate and then potentiostatically held for 5 h before impedance measurements were performed. Z-Fit of EC-lab software ® was used to fit the experimental data to an equivalent electrical circuit. The lithium diffusion coefficient was calculated using Eq. 1:

$$D = \left(\frac{V_m}{zFA}\right)^2 \left(\frac{dE}{dx}\right)^2 \left(\frac{1}{\sqrt{2}\,mA_w}\right)^2 \quad (1)$$

where V_m is the molar volume, z is the number of electrons exchanged in the redox reaction, F is Faraday's constant, A is the electrode material specific area, dE/dx is the local slope of the equilibrium E vs. x curve at the x value where impedance measurements were made, m is the

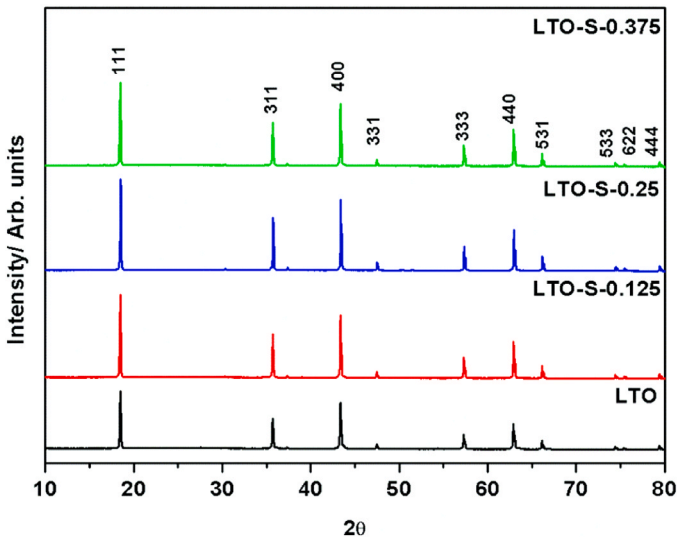

Fig. 1. XRD patterns of nominal $Li_4Ti_5O_{12}$ (LTO) and $Li_4Ti_5O_{12-x}S_x$ (LTO-S-x) with x = 0.125, 0.25 and 0.375.

Table 2
Lattice parameter *a*, cell volume of $Li_4Ti_5O_{12-x}S_x$ (x = 0, 0.125, 0.25 and 0.375) and the corresponding sulfur atomic content determined by EDS.

Sample	*a* (Å)	Volume (Å^3)	EDS: S atoms per f.u.
LTO-S-0	8.3617(3)	584.644(25)	0
LTO-S-0.125	8.3621(2)	584.718(19)	0.014 ± 0.004
LTO-S-0.25	8.3626(2)	584.836(20)	0.011 ± 0.003
LTO-S-0.375	8.3630(2)	584.923(25)	0.024 ± 0.002

electrode mass, and A_w is the Warburg coefficient. The galvanostatic intermittent titration technique (GITT) was used to determine the thermodynamic factor dE/dx. Current pulses corresponding to C/20 were applied for 30 min and the cell was then allowed to relax for 48 h or until the voltage variation was less than 1 mV/h.

The BET surface area, considered as the best approximation to the intercalation active area of electrode material, was determined by nitrogen adsorption-desorption (BET method) experiments (Micromeritics ASAP 2020 analyzer).

3. Results and discussion

3.1. Structural and morphological analysis

Fig. 1 shows the XRD patterns of synthetized $Li_4Ti_5O_{12}$ (LTO hereafter) and LTO-S-x samples (x = 0.125, 0.25 and 0.375). The diffraction patterns are fully indexed with the cubic $Li_4Ti_5O_{12}$ spinel, S.G. *Fd-3m*. The cell parameter *a* and cell volume increase only very slightly with increasing nominal sulfur content as shown in Table 2, although a much larger increase in cell volume would be expected due to the much larger size of S^{2-} (184 pm) compared to O^{2-} (140 pm) [35]. Thus, a very low degree of O/S substitution is predicted in LTO-S-x samples. Higher nominal sulfur contents such as x = 0.5 were discarded for further investigation as the XRD pattern showed the presence of a mixture of phases.

The SEM images in Fig. 2a-d show significant changes in the morphology, color, and particle size of $Li_4Ti_5O_{12}$ with nominal sulfur content. LTO has a very homogeneous granular morphology with an average size of 0.6 μm, with most of crystallites ranging between 0.2 and 0.8 μm (Fig. S1a) and a BET surface area of 0.7836 ± 0.0082 $m^2\ g^{-1}$. LTO-S-0.125 has a similar morphology and average particle size, with the majority of crystallites in the ~0.3–0.8 μm range (Fig. S1b) and a BET surface area of 4.2810 ± 0.0239 $m^2\ g^{-1}$. The main difference is that LTO also contains crystals larger than 1.2 μm. For both LTO and LTO-S-0.125, the predominance of smaller particles and the homogeneous particle distribution suggest a favorable influence on the electrochemical properties due to the shortening of the diffusion length. On the contrary, for high nominal sulfur contents, LTO-S-0.25 and LTO-S-0.375, the increasing amounts of sulfur seem to promote crystal growth and decreasing of BET surface area (for instance 0.1794 ± 0.0423 $m^2\ g^{-1}$ for x = 0.250). Note that sulfur replaces oxygen in the spinel at a significantly lower level than the nominal content. Thus, a higher surplus of sulfur may be present in instances of elevated nominal sulfur content. Formation of lithium polysulfide, with unknown melting point, and lithium sulfate, with a melting point of 859ºC, has been detected by XPS. Thus, these lithium compounds are probably melted during the reaction conditions (900 ºC under vacuum) and may function as a flux for crystal growth. Thus, for these two samples, very large inhomogeneous particles (3–15 μm) and lower BET surface areas are observed and limited kinetics are expected.

On the other hand, Fig. 2e shows SEM images with elemental mapping. All elements including sulfur are homogenously distributed. It can also be estimated that sulfur content of LTO-S-0.125 does not differ too much from that of LTO-S-0.25 while LTO-S-0.375 contains slightly more sulfur as it has been confirmed by X-EDS.

3.2. Chemical analysis

The results of the compositional analysis by X-EDS, summarized in Table 2, show that the amount of sulfur in all samples is much lower than the nominal compositions, although it increases with increasing nominal sulfur. It also shows that there is not much difference in the amount of sulfur in the LTO-S-0.125 and LTO-S-0.25, despite the difference in the nominal content and taking into account the standard deviation of sulfur content. The amount of sulfur is higher for the nominal LTO-S-0.375, but it is still extremely low compared to the nominal. This is consistent with the not very significant increase in cell parameters derived from the structural analysis, indicating that the O/S substitution occurs at much lower extent than nominal, only at the dopant level, and demonstrating that the oxygen-sulfur substitution is limited under the current synthetic Li/Ti-rich conditions.

Since interphases play a crucial role in electrochemical reactions and have a strong influence on the electrochemical properties as shown below, the amount and nature of different surface chemical species must be investigated.

3.3. Spectroscopic characterization: XPS and ATR-FTIR

Considering the importance of the surface composition, the chemical composition, and the chemical state of the elements on the surface of the prepared samples were investigated by XPS. Table 3 shows the surface chemical composition in atomic concentration (in at%) where a high carbon content is detected. The high carbon content is mainly due to adventitious contamination and to the formation of surface carbonates. The presence of small amounts of K is due to the potassium impurities in all the reactants. The Li/Ti atomic ratios of the LTO and LTO-S-0.125 samples are relatively close to the nominal Li/Ti value (0.80). However, for LTO-S-0.125, the S/Ti ratio at the surface (0.081) is higher than the nominal value (0.025), indicating the presence of sulfur-containing compounds. On the other hand, for LTO-S-0.25 and LTO-S-0.375 the Li/Ti ratios are 1.39 and 1.50, respectively, almost double the nominal value, indicating co-precipitation of lithium-containing compounds on the surface. At the same time, the S/Ti atomic ratios (0.277 and 0.721 respectively) are much higher than the nominal values (0.05 and 0.075), indicating a sulfur enriched surface. It therefore appears that the surface of these two samples may contain significant amounts of lithium sulfide or polysulfides.

Table 4 shows the binding energy values (in eV) of the different constituents and Fig. 3 the O 1 *s*, Ti 2*p* and S 2*p* core-level spectra of the

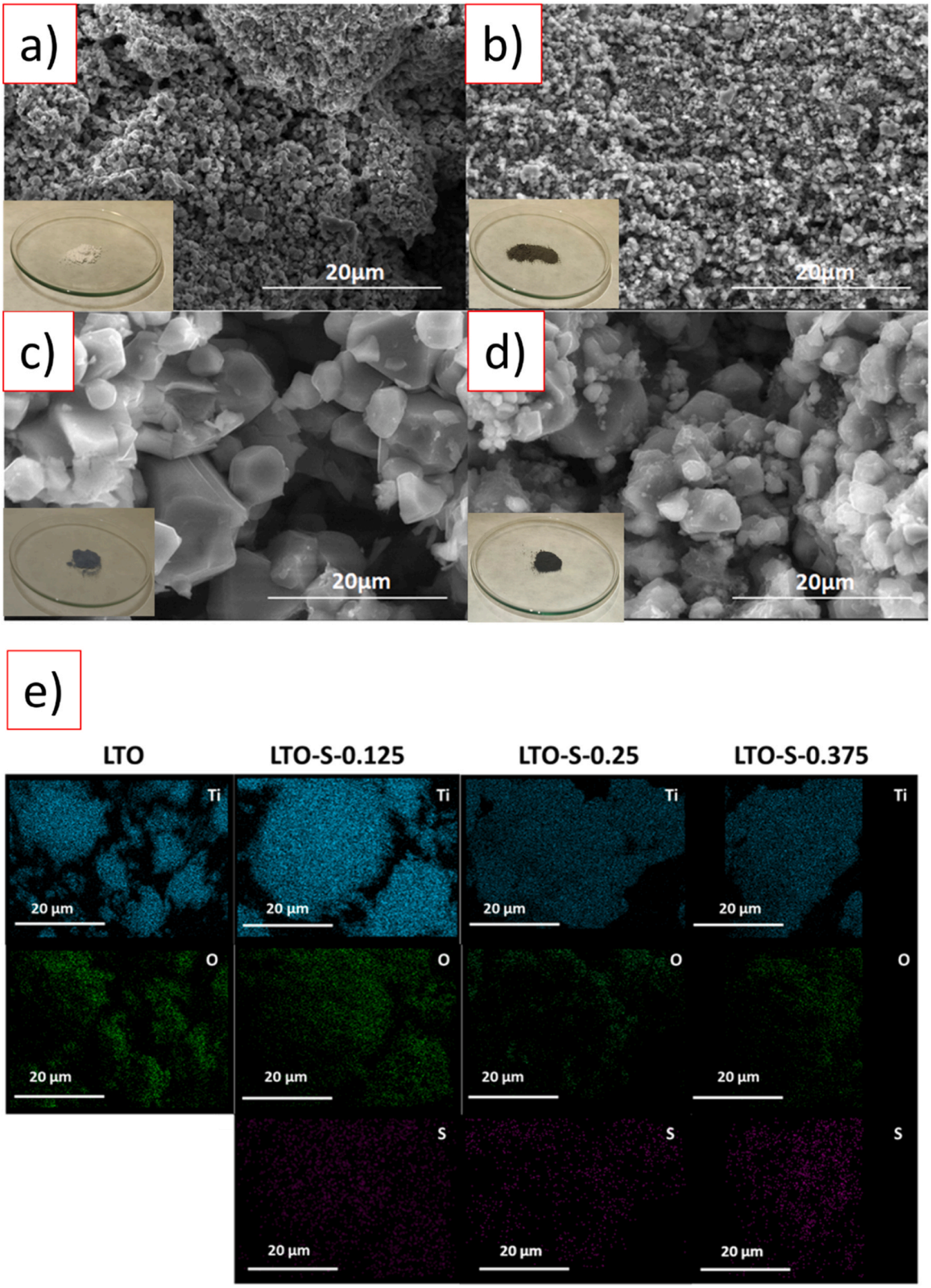

Fig. 2. SEM images of a) LTO; b) LTO-0.125; c) LTO-0.25; d) LTO-0.375; e) elemental mapping in all compositions.

studied materials. The C 1 *s* signals (Fig. S2) can be decomposed into several contributions. The main contribution at 284.8 eV is due to adventitious carbon. There are other contributions at around 286.2 eV which are attributed to C-O and C-O-C bonds. The high binding energy contribution (289.8 eV) is due to the presence of surface carbonates [35], [36]. All samples show this contribution, but it is more pronounced in the case of samples LTO-0.25 and LTO. The O 1 *s* core level signals are complex (Fig. 3) and show several contributions. The main contribution at 529.8 eV, present in all samples, is due to lattice oxygen of titanate [37], while the signal at 530.9 eV in LTO may be due to carbonate. For

Table 3
Surface chemical composition (in atomic concentration %) of the samples studied determined by XPS.

Sample	C	O	Ti	Li	S	K	Li/Ti	S/Ti	S*
LTO	14.59	55.05	17.82	11.89	–	0.64	0.67	–	–
LTO-S-0.125	43.34	34.93	11.80	7.99	0.95	0.99	0.68	0.081	0.6
LTO-S-0.25	22.54	49.61	9.70	13.53	2.69	1.93	1.39	0.277	1.2
LTO-S-0.375	46.84	32.49	6.18	9.29	4.46	0.54	1.50	0.721	1.8

S* =S nominal

Table 4
Binding energy values (in eV) of the constituent elements of the studied samples.

Sample	C 1*s*		O 1*s*		Ti $2p_{3/2}$	Li 1*s*	S $2p_{3/2}$		K $2p_{3/2}$
LTO	284.8	81%	529.8	71%	458.4	54.4	–		292.9
	286.1	13%	530.9	20%					
	289.7	6%	532.0	9%					
LTO-0.125	284.8	74%			458.3	54.4	163.0	42%	292.7
	286.2	18%	529.7	88%			166.2	5%	
	287.5	6%	531.4	12%			168.2	53%	
	289.7	2%							
LTO-0.25	284.9	90%	529.8	48%	458.4	54.8	162.5	21%	292.2
	289.9	10%	531.5	29%			166.6	6%	
			532.3	23%			168.4	73%	
LTO-0.375	284.9	77%	529.8	52%	458.4	54.5	163.1	32%	292.4
	286.7	19%	531.6	33%			167.5	16%	
	289.8	4%	532.6	15%			168.8	52%	

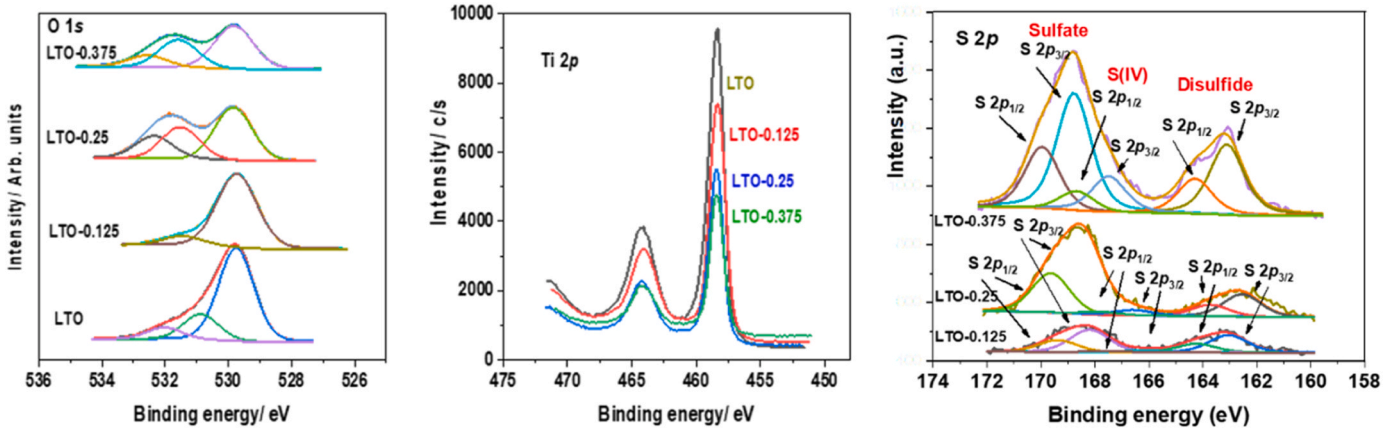

Fig. 3. O 1 *s*, Ti 2*p* and S 2*p* core level spectra for the samples studied.

the remaining LTO-S-x samples, the contributions at higher binding energies, 531.4–531.6 eV, are due to sulfate, sulfite and carbonate [38], [39]. However, these signals may also include the presence of oxygen vacancies (531.6 eV [40], as noted by Shen *et al.*[27]. The relative intensity of the signal assigned to the presence of sulfate increases with increasing S content, while no significant change in the cell parameter is observed, as mentioned above. Finally, the highest contributions above 532 eV are attributed to adsorbed water. The Ti $2p_{3/2}$ peaks have their maxima at 458.4 eV, typical for Ti(IV) in titanates [41], [42]. In all cases, the Ti $2p_{3/2}$ signal shows a perfect symmetry, and no contributions at the low binding energy side was observed. This rules out the presence of reduced titanium at the surface. All Li 1 *s* signals are centered at about 54.4 eV, typical for Li(I) [36]. More complex is the S 2*p* core level spectra (Fig. 3), where three doublets S $2p_{3/2}$-S $2p_{1/2}$ are observed. The more intense doublet shows an S $2p_{3/2}$ contribution at 168.2–168.8 eV which we attribute to sulfate. We also observe a weak doublet at 166.2–167.5 eV attributed to S(IV) species, and finally there is a relevant contribution at 162.5–163.1 eV from terminal sulfur in polysulfides in the sulfur containing samples due to disulfide formation [43]. Shen et al. [27] attributed a contribution at 168.64 eV to S(VI) replacing Ti^{4+} in the lattice, but in view of the more complex S 2*p* core level spectra

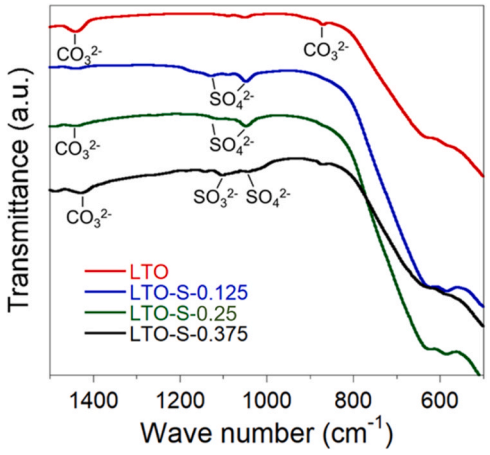

Fig. 4. ATR-FTIR spectra for LTO, LTO-S-0.125, LTO-S-0.25 and LTO-S-0.375.

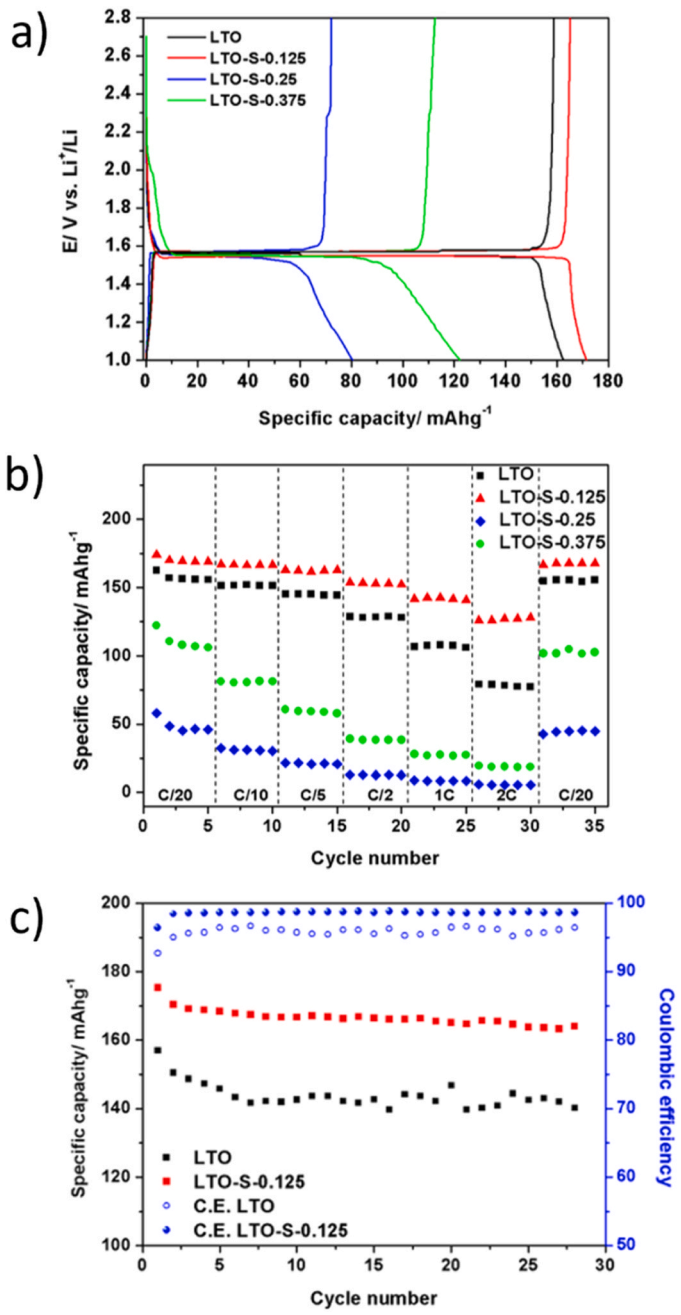

Fig. 5. a) Initial first discharge-charge curves of LTO and LTO-S samples at a rate of C/20. b) Their cycling performance at various rates. c) Cycling performance of as-prepared LTO and LTO-S-0.125 at C/5.

indicating several sulfur species, and considering that in our samples the presence of sulfate is also inferred from the O 1 *s* signal (BE > 532 eV) and the observed sulfur enrichment of the surface, the S $2p_{3/2}$ contribution at 168.2–168.8 eV was attributed to the presence of sulfate at the surface rather than S^{6+} at the Ti^{4+} site. Nevertheless, ATR-FTIR was used to discriminate between the two possibilities.

IR spectra of LTO-S-x together with undoped LTO are shown in Fig. 4. Strong IR bands below 800 cm^{-1} in all compositions are characteristic of the Ti-O spinel framework. In the IR spectrum of undoped LTO, the bands at 1440 cm^{-1} and 870 cm^{-1} are ascribed to ν_3 (ν_d, CO) and ν_2 (ν, CO_3) vibrational modes of CO_3^{2-} [44]. These vibrational modes are clearly visible in LTO-S-0.375. This finding is in agreement with XPS results, indicating a higher carbonate content. In the IR spectra of sulfur-doped compounds, a region of peaks corresponding to SO_4^{2-} (1100–1000 cm^{-1}) is observed. The two peaks at 1048 cm^{-1} and 1130 cm^{-1}, visible in LTO-S-0.125, are identified as the splitted ν_3 (ν_d) mode, due to unidentate or bidentate coordination as surface sulfate [45]. Therefore, our XPS and IR results are consistent with surface-coordinated sulfate. Within this spectral region, the higher-frequency peak may be additionally due to S-bonded SO_3^{2-}, the presence of which was confirmed by XPS. Thus, the peak seen at 1100 cm-1 in LTO-0.375 is ascribed to the ν_3 (ν_d) vibrational mode [46].

3.4. Electrochemical characterization

Fig. 5a shows the first discharge-charge cycle of the LTO, LTO-S-0.125, LTO-S-0.25 and LTO-S-0.375 samples at C/20 in the voltage range 2.8–1 V. All samples develop a plateau at 1.55 V, typical of LTO, corresponding to the two-phase process in which $Li_4Ti_5O_{12}$ transforms into $Li_7Ti_5O_{12}$, with $Ti^{4+/3+}$ being the active redox couple [47], [48]. In the case of LTO-S-0.375, a small plateau is clearly visible at 2.1 V during discharge, and which is not observed in undoped LTO. This additional process is attributed to a secondary electroactive phase. It is also present in LTO-S-0.250, although probably not as clearly seen in Fig. 5a due to its lower concentration. However, it was detected in GITT experiments (see Fig. S3). On the other hand, the absence of this process in LTO-S-0.125 suggests an even lower concentration or absence of the secondary electroactive phase. To further investigate its nature and reversibility, we have studied the reduction-oxidation processes by cyclic voltammetry performed at a fast scan rate (10 mV s^{-1}) in LTO-S-0.375 and compared with LTO (Fig. S4), demonstrating the reversibility of the process at 2.1 V. Interestingly, 32% of the sulfur content in LTO-S-0.375 was identified as disulfide by XPS, while the high surface Li/Ti ratio detected by XPS indicates a substantial formation of Li_2S_2. Consistent with this, the lower plateau in the voltage profile of Li-sulfur cells at 2.1 V is associated with the reduction process $2Li^+ + 2\ e^- + Li_2S_2 \rightarrow 2\ Li_2S$. This is in agreement with the reduction potential obtained from DFT calculations, 2.11 V [49]. Although LTO-S-0.125 has a higher percentage of surface Li_2S_2, its electroactivity is not detected in CV due to the low total amount of sulfur (S/Ti= 0.081 as shown in Table 3).

The specific capacities at C/20 of the investigated samples also show some important capacity differences as shown in Fig. 5a; LTO: 162 mAh g^{-1}, LTO-S-0.125: 172 mAh g^{-1}, LTO-S-0.25: 80 mAh g^{-1}, and LTO-S-0.375: 122 mAh g^{-1}. Interestingly, the LTO-S-0.125 sample exhibits the highest specific capacity (Fig. 5b), significantly exceeding that of LTO under identical current conditions and approaching the theoretical capacity of LTO (175 mAh g^{-1}). LTO-S-0.125 also shows excellent capacity retention with increasing current density (Fig. 5b): 167 mAh g^{-1} at C/10, 163 mAh g^{-1} at C/5, 164 mAh g^{-1} at C/2, 143 mAh g^{-1} at 1 C, 127 mAh g^{-1} at 2 C, and again exceeds the capacities of pristine LTO at the same current rates (151 mAh g^{-1}, 145 mAh g^{-1}, 128 mAh g^{-1}, 107 mAh g^{-1}, 79 mAh g^{-1}), which is particularly noticeable at high current rates. In fact, LTO-S-0.125 performs much better than any of the other samples, showing that its composition and surface favors intercalation kinetics. In addition, the cycling performance of LTO-S-0.125 is excellent, maintaining a higher capacity and a higher coulombic efficiency (close to 99%) compared to pristine LTO, as shown in the example in Fig. 5c and Fig. S5a (C/5 rate). Pristine LTO and LTO-S-0.125 deliver specific capacities of 144 mAh g^{-1} and 166 mAh g^{-1} after 50 cycles maintaining 91.7% and 95.1% of their initial specific capacities, respectively. The improvement over LTO is very significant as the capacity is very close to the theoretical capacity even at much higher currents and the capacity retention is also higher. The differences in the electrochemical properties of LTO-S-0.125 compared to samples with higher nominal sulfur content merit further examination. While the performance of LTO-S-0.125 is much better than pristine LTO, it is worse for the other samples investigated (x = 0.25 and 0.375). Interestingly, the electrochemical performance of LTO-S-0.375 is slightly better (higher capacity and better C-rate behavior, as shown in Fig. 5a and b,

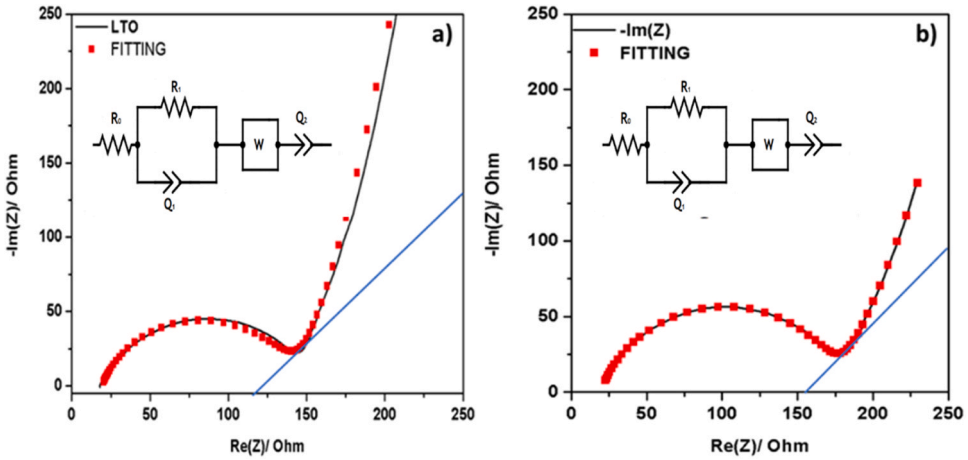

Fig. 6. Impedance spectra shown in Nyquist plots of fresh a) LTO and b) LTO-0.125 cells under a small perturbation.

when compared to LTO-S-0.25).

Since the XPS results indicates the presence of lithium on the surface forming Li_2S_2, Li_2SO_4 and Li_2SO_3 species, a possible charge compensation mechanism in the bulk $Li_{Li}^{x} + O_O^{x} + Ti_{Ti}^{x} = V_{Li}^{'} + V_O^{\bullet\bullet} + Ti_{Ti}^{'}$ is conceivable producing an oxygen and lithium deficient spinel $Li_{4-y}(Ti^{4+})_{5-y}(Ti^{3+})_yO_{12-y}$. This would explain the colour change from white in LTO to grey in LTO-S-0.125 and dark grey in LTO-S-0.250 and LTO-S-0.375 samples (See insets in Fig. 2a-d), indicating partial reduction of Ti^{4+} to Ti^{3+}. The high amount of surface Li_2SO_4, which favors the oxidation of Ti^{3+} with the concomitant reduction of SO_4^{2-} to SO_3^{2-}, would explain why no surface Ti^{3+} was detected in XPS. This is consistent with a significant amount of surface S(IV) species detected by XPS. In all samples, Li_2S formed upon reduction of Li_2S_2 is likely to coat the LTO-S crystals, although a thinner coating is expected in LTO-S-0.125. Considering that the ionic conductivity of bulk Li_2S at 25 ° C is $\sim 10^{-13}$ S cm^{-1} [50], a thicker coating will result in greater polarization, as lithium is more hindered from accessing the LTO bulk, explaining why samples with higher amounts of Li_2S_2, LTO-S-0.25 and LTO-S-0.375, perform worse. On the other hand, the larger particle size of these samples (see Fig. 2) also contributes to limiting their rate capability. To understand why LTO-S-0.375 unexpectedly performs better than LTO-S-0.25, we consider that LTO-S-0.25 has more insulating surface components (Li_2SO_4, Li_2SO_3 and Li_2CO_3) as detected in XPS.

To understand the much better performance of LTO-S-0.125 (higher capacity and capacity retention with increasing current) compared to LTO, the following main differences are as follows:

1) Expected increase in electronic conductivity in LTO-S-0.125 due to the partial reduction of Ti^{4+}, associated with reduced polarization and increased capacity as main effects. While no significant change in polarization is observed at low C/20 current (Fig. 5a), this effect is clearly noticeable during discharge-charge cycles at higher currents as shown in Fig. S5b where LTO and LTO-0.125 were cycled at high rate, C/5.
2) The presence of sulfate has no beneficial effect on rate capability, as evidenced by the poor performance of LTO-S-0.25 and LTO-S-0.375 with high amount of sulfate compared to LTO-S-0.125. In addition to insulating sulfates, electroactive surface Li_2S_2 is also present, the electronic properties of which remain unclear. However, upon discharge, Li_2S forms at ~2.1 V and may play a key role in enhancing performance due to its significant ionic conductivity ($\sim 10^{-13}$ S cm^{-1}) [51], similar to that reported for LTO [52], which allows permeation of Li^+ ions towards the bulk of LTO at a rate similar to bulk diffusion in the spinel. On the other hand, the amount of surface carbonate is higher in LTO than in LTO-S-0.125 (Table 4). Thus, the inhibitory effect on carbonation by surface passivation due to a thin Li_2S_2 layer, which is beneficial for LTO-S-0.125, cannot be excluded.
3) The BET surface area, considered as the best approximation to the effective area for intercalation, is higher in LTO-S-0.125 (4.2810 ± 0.0239 m^2 g^{-1}), than in LTO (0.7836 ± 0.0082 m^2 g^{-1}), contributing to more favorable intercalation kinetics.

Finally, resistance to lithium-ion migration and diffusion is analyzed below as a fourth key difference.

Impedance spectroscopy was used to investigate cell resistance, charge transfer and mass transport. The impedance experiments were carried out in a three-electrode Swagelok cell as described in the experimental section. This setup allows the contribution of the working electrode to be measured and avoids any impedance interference from metallic lithium. We have focused on pristine LTO and LTO-S-0.125, while the other two samples have been excluded from this analysis due to the high levels of sulfates, carbonates and sulfide that can clog the pores of the samples, resulting in specific surface area values that may not actually correspond to the effective area for intercalation as required by Eq. 1. Such interference is expected to be less in the case of LTO-S-0.125.

Fig. 6 shows the impedance response of fresh cells containing LTO and LTO-S-0.125, respectively, as the active material of the working electrode. Spectra correspond to fresh cells, this is under OCV conditions. At OCV no lithium ions are expected to be in the host. However, the AC perturbation induces lithium intercalation and deintercalation as the sign of the sinusoidal current changes. This assumption is confirmed by the presence of a mass diffusion response under the perturbation (spike). To ensure that the system remains under linear conditions the applied perturbation is small. Hence, the amount of lithium is very small, and the calculated diffusion coefficient in fresh cells is determined under dilute conditions.

Spectra at different states of discharge were also recorded in the solid solution regions and showed the same characteristic (see Fig. S6). They were all fitted with the equivalent circuit shown in the insets of Fig. 6. It consists of a typical Randles circuit [53] with an extra constant phase element (CPE) as proposed by several authors [54], [55]. The x-intercept is modelled with a resistance (R_0) which mainly corresponds to the resistance of the transport of lithium ions through the electrolyte. The mid-frequency response, where a depleted semicircle is observed, is modelled with a resistor R_1 in parallel with a constant phase element Q_1, as shown in the insets. CPE has been used as an alternative to pure capacitors to account for the relaxation frequency distribution expected for electrodes originated by the non-ideality of the electrode surface and its interface with the electrolyte (irregularities, defects, roughness, etc.) [56]. This semicircle can also be fitted with two overlapping semicircles

Table 5
Values of electrolyte resistance (R_0), CEI + CT resistance (R_1), Warburg (S) and diffusion coefficients (DLi^+) of LTO and LTO-S-0.125 at different potentials.

	LTO				LTO-S-0.125			
Voltage/ V	R_0/ Ω	R_1/ Ω	S/ Ω $s^{-1/2}$	D_{Li}/ cm^2 s^{-1}	R_0/ Ω	R_1/ Ω	S/ Ω $s^{-1/2}$	D_{Li}/ cm^2 s^{-1}
Near OCV	19.63	125.90	100.70	2.813E-11	20.54	155.6	132.67	8.287E-13
2.2	18.86	116.20	90.64	1.615E-11	21.00	115.90	107.00	1.434E-12
1.2	24.47	147.80	80.00	5.081E-14	52.96	96.17	112.00	3.132E-14
1	25.61	162.00	95.70	7.432E-14	52.78	92.73	112.50	1.098E-13

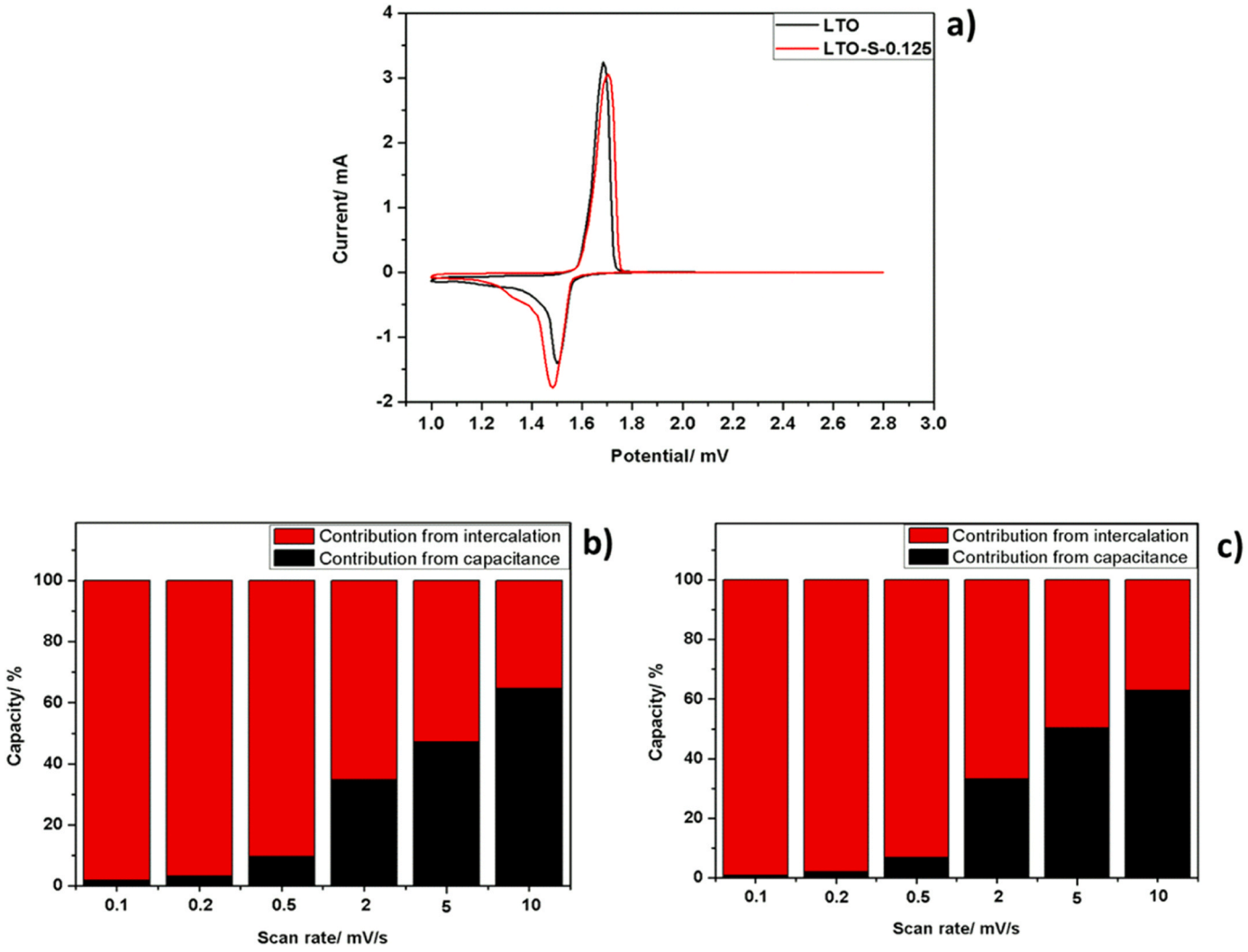

Fig. 7. a) Cyclic voltammetry of LTO and LTO-S-0.125 at 0.1 mV s^{-1}. Faradaic and capacitive processes of b) LTO and c) LTO-0.125 at different scan rates.

RQ, which can correspond to two different processes: i) resistance and capacitance of the interfaces, namely the cathode-electrolyte interface (CEI), and ii) charge transfer resistance (CT) and double layer capacitance. Although it is possible to fit the semicircle with two RQ element, the values obtained would not be reliable enough to assign individual values to each component. In our case R_1 and Q_1 therefore correspond to a total resistance and capacitance due to both phenomena. Note, however, that R_1 is usually mainly contributed by the charge transfer resistance. Finally, the region at lower frequencies corresponds to mass diffusion under semi-infinite linear conditions (modelled with a Warburg element, W) and to finite space linear diffusion at the lowest frequencies. The latter, which causes charge accumulation on the surface, can be modelled with a constant phase element (Q_2 in the equivalent circuit shown in Fig. 6). The semi-infinite linear diffusion (SILD) condition theoretically leads to a spike with 45° as in the orthonormal Nyquist plot. As a guide for the eyes, a blue straight line with a 45° slope is drawn in Fig. 6, which shows that such conditions are only fulfilled in a very narrow frequency range. This is due to the overlap of the frequency ranges corresponding to mass diffusion and charge transfer. In addition, at much lower frequencies, charge accumulation occurs on the electrode surface due to the limited kinetics of lithium diffusion [55], [57]. To model this deviation, the extra pseudocapacitor was added in series in the Randles equivalent circuit. In such cases, the value of the Warburg coefficient, A_W, is better obtained by reading the minimum of the plot of -Im(Z)* $f^{1/2}$ vs. ω for which the semi-infinite linear diffusion conditions are satisfied. As an example, Fig. S7 shows the plots based on the data of Fig. 6 and the graphical determination of the Warburg coefficient as corresponding to the minimum of -Im(Z)* $f^{1/2}$.

The fitting results are shown in Table 5 and Fig. S6. R_1, which is contributed by the interface and the charge transfer resistances, is

higher for LTO-S-0.125 (about 155 ohms) than for LTO (about 126 ohms) for the fresh cells, but it decreases during discharge. On the contrary, R1 increases for LTO and becomes higher than for LTO-S-0.125, especially at low voltage. Thus, low values of R_1 contributes to a better C-rate behavior of LTO-S-0.125.

On the other hand, taking into account Eq. 1 and the obtained values of the Warburg coefficient, the lithium diffusion coefficient, D_{Li} has been calculated at selected equilibrated potentials (see Table 5). It has only been determined in regions where the voltage varies with composition (monophasic regions), since it cannot be determined in the biphasic region (dE/dx=0) by applying Eq. 1. The values obtained indicate that diffusion of lithium is favored in LTO at OCV conditions and 2.2 V, before the onset of the two-phase region. After completion of the phase transition, the diffusion coefficients become similar in both samples.

Cyclic voltammograms of as-prepared LTO and LTO-0.125 run at very slow scan rate (0.1 mV s^{-1}) are shown in Fig. 7a. The typical cathodic peak centered at 1.5 V and the corresponding anodic peak at 1.8 V, corresponding to Li insertion/de-insertion, are clearly observed. The faradaic and capacitive contributions in the LTO and LTO-0.125 samples at different scan rates are shown in Figs. 7b and 7c. The detailed procedure is described in the Supporting Information, Fig. S8 and Table S1. LTO-0.125 and LTO have a very similar faradaic contribution at identical scan rates.

The contribution of both mass diffusion and the capacitive charge storage mechanism are unaffected by the slight reduction of Ti^{4+} and surface modification found in LTO-S-0.125. Other electrochemical signatures (sharp and well-defined oxidation-reduction peaks and a constant voltage plateau as a function of composition also confirm that LTO-S-0.125 remains a typical battery-like material similar to LTO.

4. Conclusions

In summary, S-doping in LTO under Li/Ti rich conditions, attempting to replace 0.125–0.375 out of 12 oxide ions by sulfide ions in $Li_4Ti_5O_{12}$, resulted in a low partial O/S substitution associated with a not significant increase in unit cell size as deduced from XRD. It was found that most of sulfur was deposited on the surface as SO_4^{2-} and Li_2S_2. Remarkably, a very significant improvement in performance over LTO is achieved in the nominal $Li_4Ti_5O_{12-x}S_x$ ($x = 0.125$), the LTO-S-0.125 sample. Not only does it develop 9.3% more capacity at C/20, but it also exhibits a much better power rate behavior, maintaining a capacity of 125 mAh g^{-1} at 2 C, compared to 79 mAh g^{-1} for LTO at the same rate.

Li_2S_2, formed during the high temperature reaction and detected even at low nominal sulfur contents by XPS and at higher nominal sulfur contents also by CV, is thought to be involved in preventing carbonation of the LTO-S-0.125 surface as suggested by FTIR. Although the color of the sample suggests the presence of Ti^{3+} in the bulk and would be expected as lithium deficiency produced reduction of Ti^{4+} and formation of oxygen vacancies ($Li_{4-y}(Ti^{4+})_{5-y}(Ti^{3+})_y O_{12-y}$, this was not detected on the surface. Ti^{3+} is most probably oxidized by large quantities of SO_4^{2-} present on the surface as deduced from XPS.

It appears that the improved rate capability of LTO-S-0.125 compared to LTO is not only due to the presence of Ti^{3+} and the associated improvement in electronic conductivity, but also to a surface modification with a Li_2S coating and reduced carbonation. On the other hand, the contribution of both mass diffusion and the capacitive charge storage mechanism to capacity is not affected. LTO and surface modified LTO-0.125 therefore remain typical battery-like materials.

CRediT authorship contribution statement

Julián Cáceres-Murillo: Investigation, Validation. **Pilar Díaz-Carrasco**: Methodology, Investigation, Validation. **Alois Kuhn**: Conceptualization, Methodology, Investigation, Writing –review & editing. **Enrique Rodríguez-Castellón**: Investigation, Writing –review & editing. **Flaviano García-Alvarado**: Conceptualization, Supervision, Methodology, Funding acquisition, Investigation, Writing - original draft, Project administration, Resources.

Declaration of Competing Interest

The authors declare that they have no known competing financial interests or personal relationships that could have appeared to influence the work reported in this paper.

Data Availability

Data will be made available on request.

Acknowledgments

We thank MCIN/AEI/10.13039/501100011033 for funding the projects PID2019–106662RB-C41 and PID2022–139039OB-C21. Financial support from the Universidad San Pablo CEU is also acknowledged. We are also grateful to the Comunidad de Madrid for the grant no. PEJ-2019–AI/IND-14034, which made possible the work of JC at the Universidad CEU San Pablo in the context of the "Plan de Empleo Juvenil" (Convocatoria 2019 de ayudas para la contratación de ayudantes de investigación y técnicos de laboratorio)" co-funded by European Social Fund. ERC thanks to project PID2021–126235OB-C32 funded by MCIN/AEI/10.13039/501100011033 and FEDER funds. We also thank the SCAI of the University of Málaga for the BET and XPS experiments.

Appendix A. Supporting information

Supplementary data associated with this article can be found in the online version at doi:10.1016/j.jallcom.2023.173051.

References

[1] T. Ohzuku, A. Ueda, N. Yamamoto, Zero-strain insertion material of Li [Li1 / 3Ti5 / 3] O 4 for rechargeable lithium cells, J. Electrochem. Soc. vol. 142 (5) (1995) 1431–1435, https://doi.org/10.1149/1.2048592.
[2] W. Lu, J. Liu, Y.K. Sun, K. Amine, Electrochemical performance of Li4/3Ti5/3O4/Li1+x(Ni1/3Co1/3Mn1/3)1-xO2 cell for high power applications, J. Power Sources vol. 167 (1) (2007) 212–216, https://doi.org/10.1016/j.jpowsour.2006.12.077.
[3] C.Y. Ouyang, Z.Y. Zhong, M.S. Lei, Ab initio studies of structural and electronic properties of Li4Ti5O12 spinel, Electrochem. Commun. vol. 9 (5) (2007) 1107–1112, https://doi.org/10.1016/j.elecom.2007.01.013.
[4] T. Yuan, X. Yu, R. Cai, Y. Zhou, Z. Shao, Synthesis of pristine and carbon-coated Li4Ti5O12 and their low-temperature electrochemical performance, J. Power Sources vol. 195 (15) (2010) 4997–5004, https://doi.org/10.1016/j.jpowsour.2010.02.020.
[5] C.H. Chen, et al., Studies of Mg-substituted Li4−xMgx Ti5O12 spinel electrodes (0≤x≤1) for lithium batteries, J. Electrochem. Soc. vol. 148 (1) (2001) 102–104, https://doi.org/10.1149/1.1344523.
[6] B. Yan, et al., Novel understanding of carbothermal reduction enhancing electronic and ionic conductivity of Li4Ti5O12 anode, J. Mater. Chem. A vol. 3 (22) (2015) 11773–11781, https://doi.org/10.1039/c5ta00887e.
[7] H. Yu, et al., High-rate characteristics of novel anode Li4Ti5O12/polyacene materials for Li-ion secondary batteries, Electrochim. Acta vol. 53 (12) (2008) 4200–4204, https://doi.org/10.1016/j.electacta.2007.12.052.
[8] K. Zaghib, M. Simoneau, M. Armand, M. Gauthier, Electrochemical study of Li4Ti5O12 as negative electrode for Li-ion polymer rechargeable batteries, J. Power Sources vol. 81–82 (1999) 300–305, https://doi.org/10.1016/S0378-7753(99)00209-8.
[9] Y. Wang, W. Zhu, Micro/nano-structured Li4Ti5O12 as high rate anode material for lithium ion batteries, Solid State Ion. vol. 349 (June 2019) (2020), 115297, https://doi.org/10.1016/j.ssi.2020.115297.
[10] Z. Zhang, L. Cao, J. Huang, D. Wang, J. Wu, Y. Cai, Hydrothermal synthesis of Li4Ti5O12 microsphere with high capacity as anode material for lithium ion batteries, Ceram. Int. vol. 39 (3) (2013) 2695–2698, https://doi.org/10.1016/j.ceramint.2012.09.036.
[11] H. Wu, et al., Sr-doped Li4Ti5O12 as the anode material for lithium-ion batteries, Solid State Ion. vol. 232 (3) (2013) 13–18, https://doi.org/10.1016/j.ssi.2012.10.027.
[12] R.A. Hernández-Carrillo, G. Ramos-Sánchez, G. Guzmán-González, N.A. García-Gomez, I. González, E.M. Sanchez-Cervantes, Synthesis and characterization of

iron − doped Li4Ti5O12 microspheres as anode for lithium-ion batteries, no. April 2018, J. Alloy. Compd. vol. 735 (2018) 1871–1877, https://doi.org/10.1016/j.jallcom.2017.11.218.
[13] Y.Y. Wang, Y.J. Hao, Q.Y. Lai, J.Z. Lu, Y.D. Chen, X.Y. Ji, A new composite material Li4Ti5O12- SnO2 for lithium-ion batteries, Ion. (Kiel.) vol. 14 (1) (2008) 85–88, https://doi.org/10.1007/s11581-007-0156-1.
[14] M.M. Rahman, J.Z. Wang, M.F. Hassan, S. Chou, D. Wexler, H.K. Liu, Basic molten salt process-A new route for synthesis of nanocrystalline Li4Ti5O12-TiO2 anode material for Li-ion batteries using eutectic mixture of LiNO3-LiOH-Li2O2, J. Power Sources vol. 195 (13) (2010) 4297–4303, https://doi.org/10.1016/j.jpowsour.2010.01.073.
[15] X. Guo, C. Wang, M. Chen, J. Wang, J. Zheng, Carbon coating of Li 4Ti 5O 12 using amphiphilic carbonaceous material for improvement of lithium-ion battery performance, J. Power Sources vol. 214 (2012) 107–112, https://doi.org/10.1016/j.jpowsour.2012.04.097.
[16] T.F. Yi, S.Y. Yang, X.Y. Li, J.H. Yao, Y.R. Zhu, R.S. Zhu, Sub-micrometric Li4-xNaxTi5O12 ($0 \leq x \leq 0.2$) spinel as anode material exhibiting high rate capability, J. Power Sources vol. 246 (2014) 505–511, https://doi.org/10.1016/j.jpowsour.2013.08.005.
[17] Y.J. Bai, C. Gong, Y.X. Qi, N. Lun, J. Feng, Excellent long-term cycling stability of La-doped Li4Ti 5O12 anode material at high current rates, J. Mater. Chem. vol. 22 (36) (2012) 19054–19060, https://doi.org/10.1039/c2jm34523d.
[18] N.M. Ncube, W.T. Mhlongo, R.I. McCrindle, H. Zheng, The electrochemical effect of Al-doping on Li4Ti5O12 as anode material for lithium-ion batteries, Mater. Today Proc. vol. 5 (4) (2018) 10592–10601, https://doi.org/10.1016/j.matpr.2017.12.392.
[19] W.L. Guilin Yana, Xinru Xua, Wentao Zhanga, Zhendong Liub, Preparation and electrochemical performance of P5+ doped Li4Ti5O12 as anode material for lithium-ion batteries, IOPscience vol. 31 (2021), https://doi.org/10.1088/1361-6528/ab7047.
[20] T.F. Yi, J. Shu, Y.R. Zhu, X.D. Zhu, R.S. Zhu, A.N. Zhou, Advanced electrochemical performance of Li4Ti4.95V0.05O12 as a reversible anode material down to 0 V, J. Power Sources vol. 195 (1) (2010) 285–288, https://doi.org/10.1016/j.jpowsour.2009.07.040.
[21] Z. Wang *et al.*, Preparation and Effects of Mg&Zr-doping on the Electrochemical Properties of Spinel Li 4 Ti 5 O 12 as Anode Material for Lithium Ion Battery, pp. 53–58, 2015, doi: 10.1142/9789814678971_0009.
[22] J.B. Kim, S.G. Lee, S.Y. Choi, J. Kim, S.O. Kim, Doping behavior of Br in Li4Ti5O12 anode materials and their electrochemical performance for Li-ion batteries, Ceram. Int. vol. 45 (14) (2019) 17574–17579, https://doi.org/10.1016/j.ceramint.2019.05.322.
[23] X. Bai, W. Li, A. Wei, Q. Chang, L. Zhang, Z. Liu, Preparation and electrochemical performance of F-doped Li4Ti5O12 for use in the lithium-ion batteries, Solid State Ion. vol. 324 (May) (2018) 13–19, https://doi.org/10.1016/j.ssi.2018.06.005.
[24] Y. Huang, Y. Qi, D. Jia, X. Wang, Z. Guo, W.Il Cho, Synthesis and electrochemical properties of spinel Li4Ti5O12-xCl x anode materials for lithium-ion batteries, J. Solid State Electrochem. vol. 16 (5) (2012) 2011–2016, https://doi.org/10.1007/s10008-011-1611-5.
[25] D.-D. Han, G.-L. Pan, b S. Liu, X.-P. Gao, PO4 3- doped Li4Ti5O12 hollow microspheres as anode material for lithium-ion batteries, RSC Adv. vol. 3 (2015) 10715–10722, https://doi.org/10.1039/C5RA17144J.
[26] X. Han, Z. Zhao, Y. Xu, D. Liu, H. Zhang, C. Zhao, Synthesis and characterization of F-doped nanocrystalline Li4Ti5O12/C compounds for lithium-ion batteries, RSC Adv. vol. 4 (79) (2014) 41968–41975, https://doi.org/10.1039/c4ra04953e.
[27] M. Shen, J. Zhu, S. Sun, D. Chen, F. Liu, J. Chen, Theoretical Prediction and Experimentally Realizing Cathodic Doping of Sulfur in Li4Ti5O12for Superior Lithium Storage Performance, ACS Appl. Energy Mater. vol. 4 (6) (2021) 5995–6004, https://doi.org/10.1021/acsaem.1c00845.
[28] K. Liang, X. Huang, X. Hong, Y. Liao, Y. Ren, H. Wang, Sulfur and nitrogen-doped Li4Ti5O12/rGO as an anode material for advanced sodium-ion batteries, J. Alloy. Compd. vol. 857 (2021), 158190, https://doi.org/10.1016/j.jallcom.2020.158190.
[29] D. Wang, et al., Nitrogen, sulfur Co-doped porous graphene boosting Li4Ti5O12 anode performance for high-rate and long-life lithium ion batteries, Energy Storage Mater. vol. 27 (2020) 387–395, https://doi.org/10.1016/j.ensm.2020.02.019.
[30] S. Abu Bakar, C. Ribeiro, An insight toward the photocatalytic activity of S doped 1-D TiO2 nanorods prepared via novel route: As promising platform for environmental leap, J. Mol. Catal. A Chem. vol. 412 (2016) 78–92, https://doi.org/10.1016/j.molcata.2015.12.002.
[31] J. Guo, J. Li, A. Yin, K. Fan, W. Dai, Photodegradation of rhodamine B on sulfur doped ZnO/TiO2 nanocomposite photocatalyst under visible-light irradiation, Chin. J. Chem. vol. 28 (11) (2010) 2144–2150, https://doi.org/10.1002/cjoc.201090355.
[32] M. Zhu, et al., New Method to Synthesize S-Doped TiO2 with Stable and Highly Efficient Photocatalytic Performance under Indoor Sunlight Irradiation, ACS Sustain. Chem. Eng. vol. 3 (12) (2015) 3123–3129, https://doi.org/10.1021/acssuschemeng.5b01137.
[33] C. Li, et al., Interfacial Engineered Polyaniline/Sulfur-Doped TiO2 Nanotube Arrays for Ultralong Cycle Lifetime Fiber-Shaped, Solid-State Supercapacitors, ACS Appl. Mater. Interfaces vol. 10 (21) (2018) 18390–18399, https://doi.org/10.1021/acsami.8b01160.
[34] J. Rodriguez-Carvajal, Program FULLPROF, Phys. B., vol. 192, no. 55, 1993.
[35] R.D. Shannon, C.T. Prewitt, Effective ionic radii in oxides and fluorides, Acta Crystallogr. Sect. B Struct. Crystallogr. Cryst. Chem. vol. 25 (5) (1969) 925–946, https://doi.org/10.1107/s0567740869003220.
[36] D.J. Morgan, Comments on the XPS Analysis of Carbon Materials, J. Carbon Res. vol. 7 (3) (2021) 51, https://doi.org/10.3390/c7030051.
[37] K.N. Wood, G. Teeter, XPS on Li Battery Related Compounds: Analysis of Inorganic SEI Phases and a Methodology for Charge Correction, ACS Appl. Energy Mater. (2018), https://doi.org/10.1021/acsaem.8b00406.
[38] M. Ishfaq *et al.*, interface 1. 5 MeV proton irradiation effects on electrical and structural properties of TiO 2 / n-Si interface, vol. 174506, 2014, doi: 10.1063/1.4874942.
[39] M. Wahlqvist, A. Shchukarev, XPS spectra and electronic structure of Group IA sulfates, J. Electron Spectros. Relat. Phenom. vol. 156–158 (2007) 310–314, https://doi.org/10.1016/j.elspec.2006.11.032.
[40] L. Xu, et al., Plasma-Engraved Co3O4 Nanosheets with Oxygen Vacancies and High Surface Area for the Oxygen Evolution Reaction, Angew. Chem. - Int. Ed. vol. 55 (17) (2016) 5277–5281, https://doi.org/10.1002/anie.201600687.
[41] V. Pfeiferab, et al., In situ observation of reactive oxygen species forming on oxygen-evolving iridium surface, Chem. Sci. (2016), https://doi.org/10.1039/C6SC04622C.
[42] L. Marchetti, F. Miserque, M. Pijolat, XPS study of Ni-base alloys oxide films formed in primary conditions of pressurized water reactor, no. Febr. (2015), https://doi.org/10.1002/sia.5757.
[43] M. Fantauzzi, B. Elsener, D. Atzei, A. Rigoldi, A. Rossi, Exploiting XPS for the identification of sulfides and polysulfides, RSC Adv. vol. 5 (93) (2015) 75953–75963, https://doi.org/10.1039/c5ra14915k.
[44] S. Koda, S. Ooi, H. Kuroya, Y. Nakamura, S. Kawaguchi, Crystal structure of a molecular complex of acetylacetone with manganese(II) bromide, MnBr2(C5H8O 2)2, *J. Chem. Soc. D. Chem. Commun.*, no. (7) (1971) 280–281, https://doi.org/10.1039/C29710000280.
[45] P.C.H. MITCHELL and R.J.P. WILLIAM, The Infrared Sjpectra and General Properties of Inorganic Thiocyanates, no. 382, pp. 1912–1918, 1960.
[46] G. Newman, D.B. Powell, The infra-red spectra and structures of metal-sulphite compounds, Spectrochim. Acta vol. 19 (1) (1963) 213–224, https://doi.org/10.1016/0371-1951(63)80100-9.
[47] S. Scharner, W. Weppner, P. Schmid-Beurmann, Evidence of Two-Phase Formation upon Lithium Insertion into the Li1.33Ti1.67 O 4 Spinel, J. Electrochem. Soc. vol. 146 (3) (1999) 857–861, https://doi.org/10.1149/1.1391692.
[48] J. Shu, Electrochemical behavior and stability of Li 4Ti 5O 12 in a broad voltage window, J. Solid State Electrochem. vol. 13 (10) (2009) 1535–1539, https://doi.org/10.1007/s10008-008-0723-z.
[49] Z. Feng, C. Kim, A. Vijh, M. Armand, K.H. Bevan, K. Zaghib, Unravelling the role of Li2S2in lithium-sulfur batteries: A first principles study of its energetic and electronic properties, J. Power Sources vol. 272 (2014) 518–521, https://doi.org/10.1016/j.jpowsour.2014.07.078.
[50] Z. Lin, Z. Liu, N.J. Dudney, C. Liang, L.I.T. Al, Lithium superionic sulfide cathode for all-solid lithium-sulfur batteries, ACS Nano no. 3 (2013) 2829–2833.
[51] I.A. Stenina, A.B. Il, A.B. Yaroslavtsev, Synthesis and ionic conductivity of Li 4 Ti 5 O 12, Inorg. Mater. vol. 51 (1) (2015) 62–67, https://doi.org/10.1134/S0020168515010185.
[52] V. Gorshkov, N. Mukhina, B. Tsarev, D. Kellerman, Electronic conductivity control in lithium titanate, ECS Meet. Abstr. vol. MA2009–02 (7) (2009), https://doi.org/10.1149/ma2009-02/7/463.
[53] C. Ho, I.D. Raistrick, R.A. Huggins, Application of A-C techniques to the study of lithium diffusion in tungsten trioxide thin films, J. Electrochem. Soc. vol. 127 (2) (1980) 343–350, https://doi.org/10.1149/1.2129668.
[54] M. Casas-Cabanas, et al., Crystal chemistry of Na insertion/deinsertion in FePO 4-NaFePO 4, J. Mater. Chem. vol. 22 (34) (2012) 17421–17423, https://doi.org/10.1039/c2jm33639a.
[55] K. Adams, A.F. González, J. Mallows, T. Li, J.H.J. Thijssen, N. Robertson, Facile synthesis and characterization of Bi13S18I2 films as a stable supercapacitor electrode material, J. Mater. Chem. A vol. 7 (4) (2019) 1638–1646, https://doi.org/10.1039/c8ta11029h.
[56] J.I. Yamaura, M. Isobe, H. Yamada, T. Yamauchi, Y. Ueda, Low temperature X-ray study of β-AxV2O5, J. Phys. Chem. Solids vol. 63 (6–8) (2002) 957–960, https://doi.org/10.1016/S0022-3697(02)00082-3.
[57] D.J. Kim, et al., Diffusion behavior of sodium ions in Na0.44MnO2 in aqueous and non-aqueous electrolytes, J. Power Sources vol. 244 (2013) 758–763, https://doi.org/10.1016/j.jpowsour.2013.02.090.